A Reductive Environment-Assisted Dealloying Approach for Hierarchical Porous Metals in Efficient Magnesium Metal Batteries

Jun-Won Lee+,[a] YongJun Cho+,[b] Hyeonmin Jo,[a] Hee Seung Ryu,[a] Eun Seon Cho,*[b] and Hee-Dae Lim*[a, c]

This study introduces monolithic three-dimensional nanoporous magnesium (3D-NPMg) fabricated through a scalable solution-based dealloying process as electrodes. By employing a naphthalene-based reductive environment, this approach forms a hierarchically porous 3D structure with clean metallic surfaces, thereby forming a free-standing 3D bicontinuous nanostructure. The resulting 3D-NPMg addresses critical challenges in magnesium metal battery (MMB) anodes, including high polarization, dendritic growth, and limited cycling stability. Electrochemical performance tests show that 3D-NPMg exhibits lower overpotentials, improved charge-transfer kinetics, and a significantly extended cycling life. The interconnected porous structure facilitates efficient ionic transport and uniform Mg deposition, thus suppressing volume expansion and reducing top-plating during cycling. With its rapid oxidation-minimizing synthesis, this solution-based dealloying process offers broad applications across various metals, which can advance the development of stable, high-performance anodes for next-generation MMBs.

Introduction

Lithium-ion batteries (LIBs) have dominated most energy storage applications; however, there is an ever-increasing need to improve energy storage technologies to achieve longer cycle lives, higher energy densities, lower costs, and greater material sustainability. For example, the success of electric vehicles (EVs) depends on enhancing their energy density to extend the driving range of a single charge.[1] More importantly, the large-scale batteries used in EVs and energy storage systems (ESS) require a significant reduction in cost.[2] This highlights the urgent need for alternatives to the limited sources of lithium (Li) metal. Consequently, researchers are investigating non-Li metal anodes as potential replacements, with the aim of utilizing more abundant materials.[3]

Among alternative metals, magnesium (Mg) has recently emerged as a promising option. Mg metal has been utilized as an anode for reversible magnesium metal batteries (MMBs) because it provides advantages such as a high energy density, abundant resources, safety, and cost-effectiveness.[4] In terms of volumetric energy density, MMBs are capable of delivering a huge capacity of 3,833 WhL^{-1}, which far exceeds that of Li metal (2,062 WhL^{-1}).[5] This advantage strengthens the potential of MMBs for use in ESS, where limited space and compact volume are critical, while weight is less important. However, several issues currently limit the commercialization of MMBs, including the lack of ideal electrolyte and cathode materials. Fortunately, since the first report of reversible MMBs with non-aqueous electrolytes,[6] many researchers have proposed suitable cathodes, such as Mo_6S_8[3a] and V_2O_5,[7] as well as electrolytes such as all-phenyl complex (APC),[8] magnesium aluminum chloride complex (MACC),[9] and $Mg(BH_4)_2$,[10] all of which have demonstrated promising performance.

Despite these advancements, the most critical limitation lies in the Mg metal anode itself; the formation of a passive film at the anode–electrolyte interface leads to high polarization, slow kinetics, poor cyclability, and dendrite formation.[11] Numerous strategies have been proposed to improve the Mg metal interface with the aim of enhancing the Mg ion conduction and activating the surface in contact with ether-based electrolytes.[12] Additionally, recent strategies have focused on reducing the effective current density by designing a three-dimensional (3D) host to achieve improved kinetics, particularly for anode-free MMBs.[13] Unfortunately, typical current collectors are difficult to use in common APC electrolytes owing to corrosion issues. Although corrosion-resistant designs are possible, scaling them for practical applications remains challenging. Considering that a 3D scaffold can effectively reduce the local effective current density, aiding the suppres-

[a] J.-W. Lee,+ H. Jo, H. S. Ryu, H.-D. Lim
Department of Chemical Engineering, Hanyang University, Hanyang University, Seoul, 04763, Republic of Korea
E-mail: junwonlee@hanyang.ac.kr
lak22222@hanyang.ac.kr
hsryu@hanyang.ac.kr
hdlim@hanyang.ac.kr

[b] Y. Cho,+ E. S. Cho
Department of Chemical and Biomolecular Engineering, Korea Advanced Institute of Science and Technology (KAIST), Daejeon, 34141, Republic of Korea
E-mail: choyj8503@kaist.ac.kr
escho@kaist.ac.kr

[c] H.-D. Lim
Department of Battery Engineering, Hanyang University, Seoul, 04763, Republic of Korea
E-mail: hdlim@hanyang.ac.kr

[+] J.-W. Lee and Y. Cho contributed equally to this work and should be considered as co-first authors.

📖 Supporting information for this article is available on the WWW under https://doi.org/10.1002/batt.202400749

Batteries & Supercaps

Research Article
doi.org/10.1002/batt.202400749

Chemistry
Europe

European Chemical
Societies Publishing

sion of dendritic growth, the use of porous Mg metal is considered an ideal approach and has attracted considerable interest.[14]

However, the fabrication of porous Mg metal is technically challenging, primarily because of difficulties in controlling the material and its tendency to oxidize during synthesis or cell fabrication. The extensively exposed surfaces of nanoporous metals are prone to oxidation, leading to significant interfacial resistance.[15] This is particularly problematic for multivalent ions such as Mg^{2+} and Zn^{2+}, which have strong interactions with anion neighbors in the passivation layer, thus severely hindering ion transport and resulting in high polarization.[16] Therefore, a new method is required to produce high-quality nanoporous Mg metal with minimal surface oxidation.

In this study, we demonstrate a free-standing 3D bicontinuous nanostructure of Mg metal fabricated from a solution-based dealloying for use as an MMB anode. This nanoporous Mg structure featuring interconnected pores is formed in a reductive environment that effectively minimizes surface oxidation and alleviates the high overpotentials typically associated with surface passivation layers. This scalable solution-based approach is both faster and more practical than conventional dealloying techniques.[17] The resulting 3D-NPMg structure reduces the overpotential and improves the cycling stability by promoting uniform Mg deposition and enhancing the ion diffusion kinetics. This method can provide an efficient and stable platform for Mg deposition, addresses the key challenges in MMBs, and offers a promising approach for future applications.

Results and Discussion

For energy applications, including MMBs, it is important to maintain the metallic surface of the Mg, which is prone to passivation, even in protective environments such as glove boxes.[18] Therefore, we prepared porous metallic Mg through a straightforward chemical treatment involving solution-phase selective Li dissolution.[17] $Mg_{15}Li_{85}$ alloy foil was cut into circular discs and immersed in a naphthalene solution (Figure 1a). This simple chemical treatment enabled the selective removal of Li, resulting in a porous Mg structure with an exposed metallic surface. This synthetic strategy offers several advantages for minimizing the oxidation of the resulting nanoporous Mg. First, the byproduct of dealloying, lithium naphthalenide, is a strong reducing agent that protects the ligaments during dealloying.[19] Second, the significantly shorter reaction time compared with other conventional methods reduces potential contamination from the external environment.[20] More importantly, this solution-based dealloying process does not require a harsh environment or specialized equipment, making it highly scalable and promising for the mass production of monolithic 3D nanostructured MMB anodes. Building on these advantages, we used the prepared 3D-NPMg as an anode host for MMBs. As shown in Figure 1b, conventional 2D Mg foils tend to allow Mg metal deposition on the top surface, leading to undesirable dendritic growth and cell short circuits.[21] In contrast, we expect

that this unique metal design will be advantageous for accommodating Mg metal within the host owing to the significantly reduced local current density, resulting in improved electrochemical performance.

As an initial step, we analyzed the dealloying of Li from the $Mg_{15}Li_{85}$ parent alloy. X-ray diffraction (XRD) analysis was performed to examine the crystallography of the fabricated 3D-NPMg (Figure 1c). After the dealloying process, the pristine $Mg_{15}Li_{85}$ alloy (bcc) peaks clearly disappeared, while the 3D-NPMg exhibited pure Mg metal (hcp) peaks that closely matched those of reference JCPDS #35-0821. The reference Mg foil predominantly exhibited a preferred orientation of the (002) plane, which is known to have the lowest surface energy and conducive to dense and dendrite-free Mg deposition.[22] In contrast, the 3D-NPMg showed vertical preferred orientations along the (101), (110), and (100) planes. These unconventional orientations are likely influenced by the rapid dissolution and nucleation processes during the dealloying procedure, which may favor kinetically driven crystal growth rather than equilibrium-based formation of the (002) plane.[23] Additionally, the high surface area and grain boundaries introduced by the nanoporous structure of 3D-NPMg could play a role in stabilizing these higher-index planes under non-equilibrium conditions.[24] This result demonstrates that Li was effectively chemically dissolved, leaving behind nearly pure nanosized Mg after the solution-based dealloying process, and no detectable oxides or hydroxides were formed during synthesis.

The nanoporous morphology of 3D-NPMg was also examined using scanning electron microscopy (SEM). As shown in Figure 1d, the Li-selective dealloying process successfully produced a bicontinuous porous Mg framework. The inset highlights the nanostructured porous morphology, with identifiable nanoscale ligaments. These nanostructures were evenly distributed throughout the anode, exhibiting rough surfaces in the cross-sectional image (Figure S1). Notably, interconnected nanopores of approximately 20–50 nm in diameter were uniformly distributed throughout the metal structure. We believe that this high level of uniformity highlights the advantages of solution-based synthesis for the production of nanoporous Mg metal. The high surface area and electrochemically active metallic character are expected to support effective Mg metal accommodation during electrochemical plating.

To further investigate the surface structure of 3D-NPMg, transmission electron microscopy (TEM) images of the ligaments were obtained (Figure 1e). Although crystalline MgO was not detected in the XRD patterns, a thin polycrystalline MgO layer passivating the Mg ligaments was observed in the TEM images. The passivation layer was less than 5 nm thick, which is sufficiently thin to preserve the electrochemical activity of the Mg surface. The observed *d*-spacing of the nanoporous Mg was consistent with that of pure Mg, indicating nearly complete Li removal during dealloying. High-angle annular dark-field (HAADF) images also confirm that the metallic Mg surface remained largely intact within the 3D framework (Figure S2).

In Figure 2a, the photograph of the Mg foil shows a silver-colored surface due to light reflection, and the corresponding SEM image reveals a flat, smooth top surface. This flat Mg foil
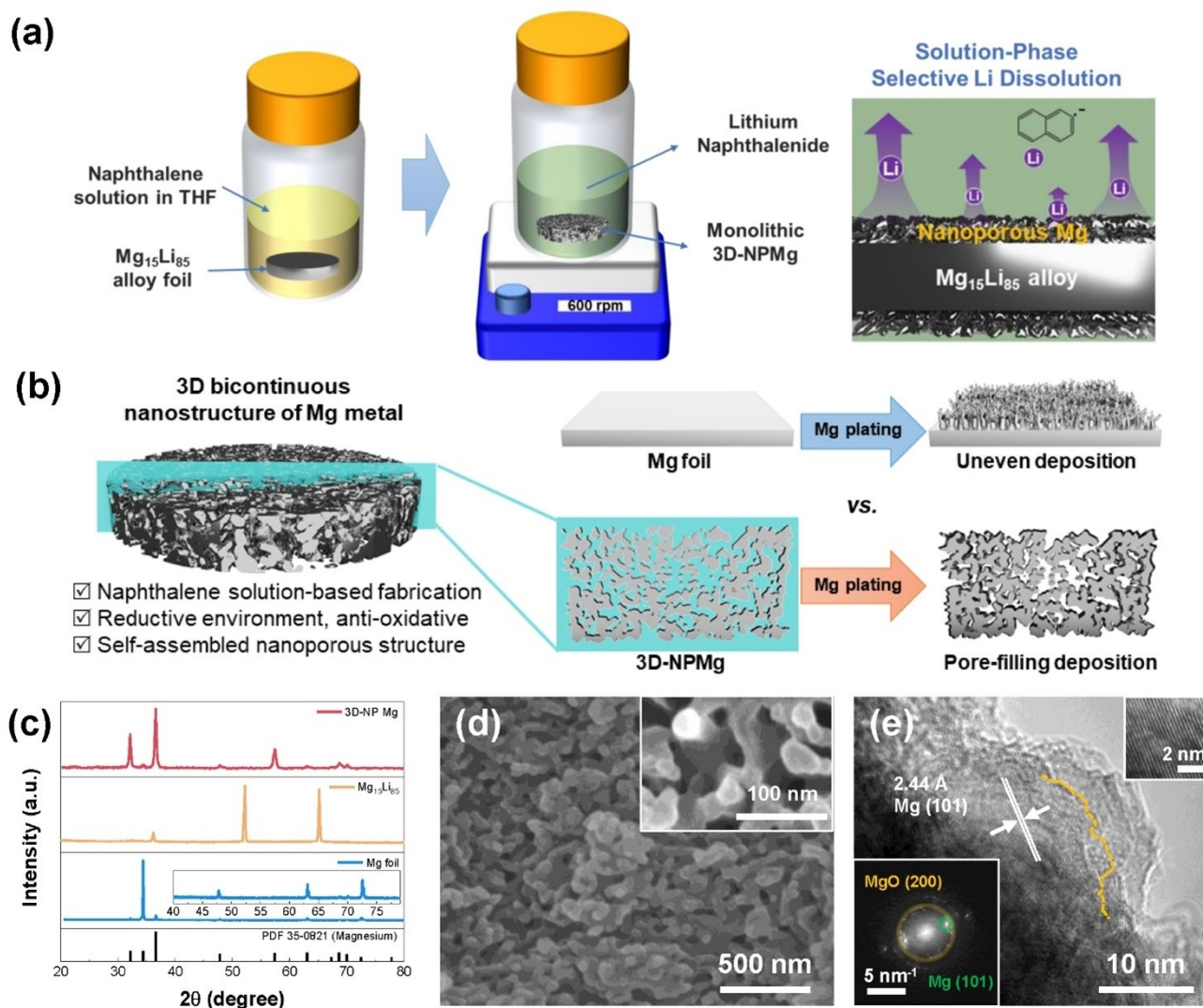
Figure 1. (a) Schematic illustration of the preparation of 3D-NPMg via the chemical dealloying process. (b) Application strategy for using 3D-NPMg in efficient MMBs. (c) XRD patterns of Mg foil, Mg–Li alloy, and 3D-NPMg. (d) SEM images and (e) TEM images and corresponding FFT pattern of 3D-NPMg. The yellow line indicates the boundary between metallic Mg and the passivation layer. The upper-right inset indicates the cropped image of lattice patterns of Mg.

has been reported to cause uneven Mg seed formation, leading to problematic Mg dendrites.[11d,13c,25] In contrast, 3D-NPMg has a darker surface color because of its light-absorbing nanoporous structure, which scatters light in multiple directions and reduces direct reflection. Light becomes trapped in the numerous pores, leading to absorption rather than reflection, thus producing a darker appearance. The SEM image of 3D-NPMg in Figure 1d further confirms its highly porous structure, lacking any flat surfaces. Notably, the disc shape of the parent alloy was retained after dealloying, resulting in a monolithic nanoporous structure that is well-suited for MMB anode applications.

To determine the pore volume and surface area of the 3D-NPMg accurately, N_2 sorption isotherms were recorded and analyzed using the Brunauer–Emmett–Teller (BET) and Barrett–Joyner–Halenda (BJH) methods, as shown in Figure 2b. The isotherm resembles a Type IV(a) isotherm with hysteresis, indicating that capillary condensation upon N_2 adsorption resulted owing to the presence of mesopores[26]; similar

isotherm types have been reported for various nanoporous metals.[27] Notably, a relatively high surface area (65.9 m^2/g) was measured for 3D-NPMg, with clear pore distributions smaller than 50 nm, which is consistent with the morphology observed in the SEM images. This suggests that the Li dealloying process with naphthalene effectively generated uniform nanopores within the 3D Mg metal structure.

Fourier transform infrared spectroscopy (FTIR) and temperature-programmed desorption coupled with mass spectroscopy (TPD-MS) were performed to investigate residual molecules on the surface from the synthesis process (Figure S3), in which neither residual solvent (THF) nor naphthalene was not detected, indicating that the molecules were effectively removed during synthesis.

To assess the surface structure of 3D-NPMg, X-ray photoelectron spectroscopy (XPS) measurements were conducted on both the Mg foil and 3D-NPMg samples. For the Mg foil (Figure 2c), the oxidative passivation peak (Mg–O) was detected
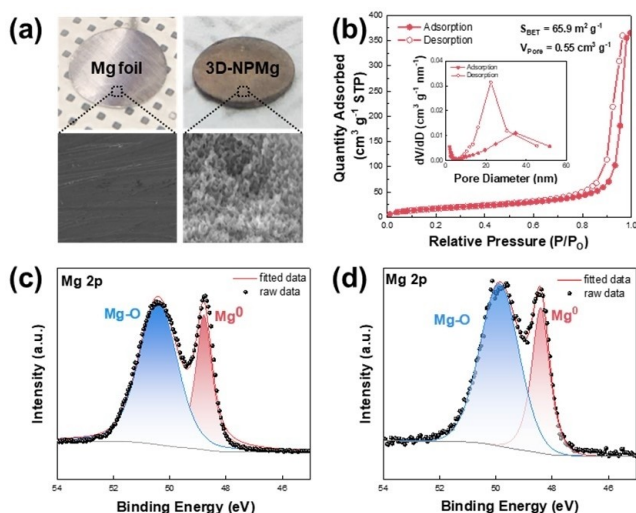
Batteries & Supercaps

Research Article
doi.org/10.1002/batt.202400749

Chemistry
Europe

European Chemical
Societies Publishing

Figure 2. (a) Photographs and corresponding SEM images of Mg foil and 3D-NPMg. (b) Nitrogen adsorption/desorption isotherms and BJH pore size distributions of 3D-NPMg. High-resolution XPS spectra of Mg 2p for (c) Mg foil and (d) 3D-NPMg. XPS spectra were corrected using 285.0 eV of C 1s adventitious carbon period

alongside the metallic Mg^0 peak. Similarly, 3D-NPMg (Figure 2d) exhibited comparable peak intensities, indicating that despite its highly porous structure, which could potentially facilitate oxidative passivation upon exposure to oxygen sources, the degree of passivation observed was similar to that of the bare Mg foil. It should be noted that the presence of electronegative Li on the surface of 3D-NPMg can shift the peaks to the lower binding energy compared to the pure Mg foil.[17,28] Given the probing depth of XPS—approximately a few nanometers—along with the TEM observations, the passivation layer was sufficiently thin to detect the metallic fraction of the Mg ligament. This suggests that despite the high specific surface area and curvature resulting from nanosizing, the 3D-NPMg exhibited a lower degree of oxidation. Normally, nanoporous metal structures exhibit a higher level of surface defects, which may contribute to greater passivation of the ligaments.[29] However, we noted that the reductive environment-assisted environment effectively inhibited oxidation during 3D-NPMg synthesis. The effect of treatment time on the degree of oxidation is shown in Figure S4.

We investigated the morphological changes upon Mg deposition for both the Mg foil and 3D-NPMg. The pristine Mg foil has a smooth surface morphology in the top view (Figure 3a), which inherently promotes uneven top-plating of electro-deposited Mg metal, as observed in Figure 3b and c. The agglomeration of the deposited Mg causes variations in the ionic flux, creating sites conducive to dendritic growth. Recently, the dendritic growth of Mg metal, which can lead to cell short circuits, has been reported as a critical limitation of MMBs.[30] Notably, both volume expansion and top-plating can be suppressed in 3D-NPMg owing to its unique porous structure, as shown in the side view (Figure 3d). This nanoporous architecture significantly reduces the local current density by providing a larger active surface area, while the anti-

oxidative conditions help maintain clean surfaces for Mg deposition. Consequently, even after the same electro-deposition of Mg (Figure 3e), no agglomeration was observed, and the hollow structure remained intact and active. While the Mg foil exhibited top-plating of Mg, 3D-NPMg accommodated the Mg metal without dendritic top growth, facilitating uniform deposition within the interior of the host (Figure 3f).

To assess the Mg accommodation capability of 3D-NPMg, we measured the ligament widths in both the as-prepared and Mg-plated 3D-NPMg. The ligaments in the as-prepared 3D-NPMg were centered around a size of approximately 37 nm (Figure 3g). After Mg plating, the ligament size increased statistically from 37.3 to 54.1 nm, indicating the capacity of the structure to accommodate plated Mg (Figure 3h). This increase in ligament width reflects the structural adaptability of 3D-NPMg to Mg deposition, which is expected to enhance its performance as an accommodating anode material for MMBs.

We conducted a detailed electrochemical performance analysis of 3D-NPMg in comparison with that of Mg foil. Electrochemical impedance spectroscopy (EIS) was performed over a frequency range of 50 mHz to 1 MHz for each symmetric cell configured with Mg foil and 3D-NPMg (Figure 4a and b). Nyquist plots for both materials were recorded in their pristine states and after 100 cycles, with the corresponding equivalent circuits shown in the insets. The symmetric cells fabricated with Mg foil (Figure 4a) exhibited large semicircles and high charge-transfer resistance (R_{ct}), indicating significant interfacial resistance in the kilo-ohm range. This was attributed to the unavoidable formation of a native oxide layer on the Mg foil. Commercial Mg metals suffer from this native oxide layer, and kilo-ohm-scale resistances have been observed for as-prepared Mg cells.[31] Even after 100 cycles, a high interfacial resistance remained, indicating that the highly resistive passivation layer continued to hinder the Mg ion diffusion. In contrast, the EIS results for 3D-NPMg (Figure 4b) showed a distinctly different behavior. The pristine 3D-NPMg exhibited a much lower charge-transfer resistance, with a high-frequency semicircle value of 23.1 Ω, likely due to the active interfaces created in the naphthalene-based reductive environment. Additionally, considering the similar level of passivation layer compared to the Mg foil, the characteristic nanostructure of 3D-NPMg also contributes the much less R_{ct} value of 3D-NPMg.

Notably, after 100 cycles, the total resistance (R_{ct}) increased only slightly from 23.1 to 74.2 Ω, indicating that the ion-conducting interphase layer remained well-preserved in the 3D-NPMg. These EIS results demonstrate the enhanced interfacial ionic transport and superior stability of 3D-NPMg over prolonged cycling.

To examine the impact of the nanoporous structure of 3D-NPMg in more detail, we compared the nucleation overpotentials during initial Mg deposition on the Mg foil and 3D-NPMg, as shown in Figure 4c. Each half-cell was configured with an Mg metal counter, and deposition onto each host was conducted at 1 mA cm^{-2}. The nucleation overpotential of the Mg foil was 248 mV, whereas the 3D-NPMg exhibited a significantly lower value of 43 mV. This reduction can be attributed to the unique nanoporous structure of 3D-NPMg,
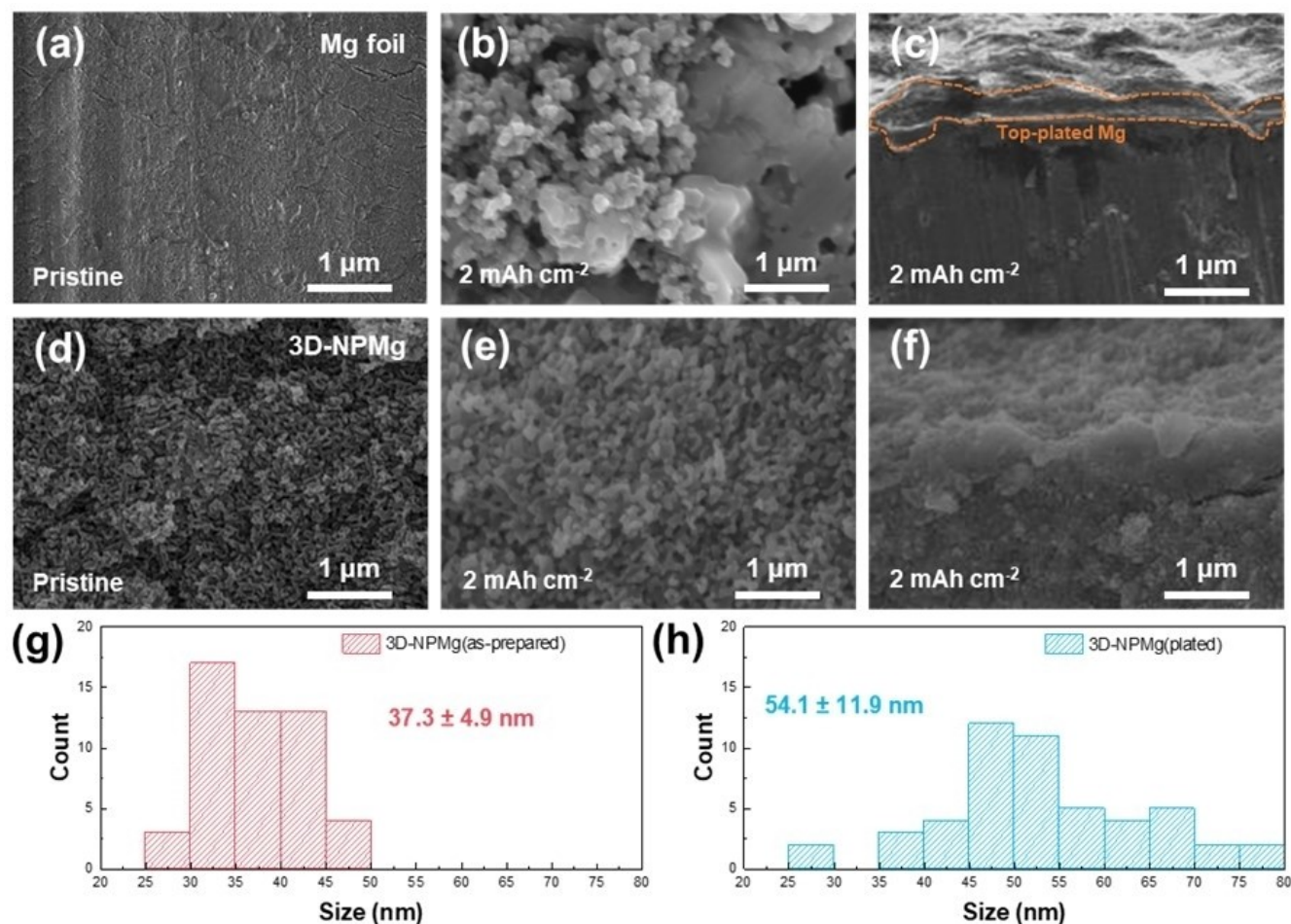
Figure 3. SEM images of pristine anodes of (a) Mg foil and (d) 3D-NPMg. Top-view SEM images of (b) Mg foil and (e) 3D-NPMg after Mg deposition to 2 mAh cm^{-2} at 2 mA cm^{-2}, with corresponding cross-sectional SEM images of (c) Mg foil and (f) 3D-NPMg. Size distributions of Mg ligaments in 3D-NPMg measured in the (g) as-prepared specimen and (h) specimen after Mg plating. Ligament size distributions were determined manually using ImageJ software, focusing on the thickness of the necks at the central (thinnest) regions for measurement.

which effectively reduces local current densities. Tafel plots for symmetric cells (Figure 4d) were also examined to evaluate the charge transfer kinetics influenced by the metal host designs and to quantify the exchange current density (ECD, j_0) of the Mg^{2+}/Mg redox reaction. ECD is a key metric for assessing the intrinsic kinetics of the electron transfer at the electrode surface[32]; a higher ECD reflects a more rapid reaction. Remarkably, the 3D-NPMg exhibited an ECD several orders of magnitude higher than that of Mg foil. This elevated ECD accounts for the significantly lower R_{ct} and nucleation overpotential because a lower overpotential is required to initiate the electrochemical reaction. The relatively rapid ion diffusion kinetics at the electrolyte/electrode interfaces facilitate smooth and uniform Mg deposition, as illustrated in the SEM images.

To evaluate the cycling performance of each metal host, cycling tests were conducted at a current density of 2 mA cm^{-2} to a limited capacity of 2 mAh cm^{-2}. The Mg plating/stripping behavior was assessed using symmetric cycling tests (Figure 4e). The Mg foil exhibited high polarization and unstable cycling profiles, leading to a shortened cycle life. After approximately 80 h, a sudden short circuit occurred, causing the voltage to

drop to nearly zero with no further changes in the cycling behavior. In contrast, 3D-NPMg exhibited a significantly lower polarization, which remained stable over 450 h. The 3D-NPMg exhibited reduced overpotentials and steady voltage profiles, indicating a much longer cycle life. These results suggest that the nanoporous 3D structure of 3D-NPMg fabricated in an anti-oxidative environment can substantially improve its electrochemical performance.

Conclusions

In this study, we exploited three-dimensional nanoporous Mg metal (3D-NPMg) fabricated in a scalable and solution-based method as a high-performance anode for MMBs. This approach effectively minimizes surface oxidation in porous metals through a naphthalene-based reductive environment, yielding a hierarchically porous Mg structure that markedly enhances the electrochemical performance. The 3D-NPMg design reduces local current densities, lowers overpotentials, and facilitates uniform Mg deposition, thus effectively suppressing top-plating
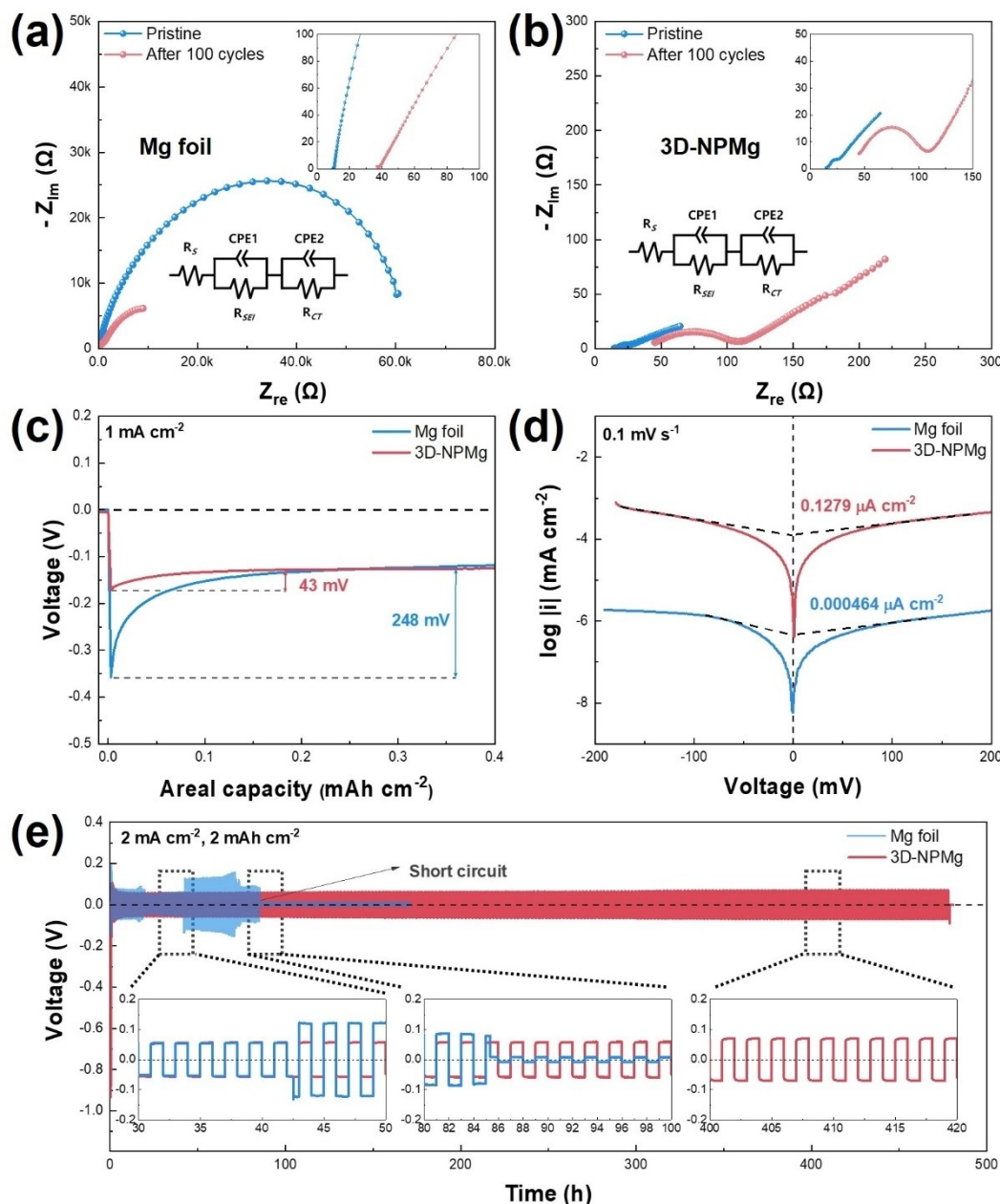
Figure 4. Nyquist plots for symmetric cells composed of (a) Mg foil and (b) 3D-NPMg in pristine condition and after 100 cycles. (c) Nucleation overpotential of Mg foil and 3D-NPMg measured at a current density of 1 mA cm^{-2}. (d) Tafel plots and (e) galvanostatic cycling of each symmetric cell at 0.2 mA cm^{-2}.

and enhancing cycling stability. Electrochemical analyses confirmed the improved ionic transport, stable charge-transfer kinetics, and extended cycling life achieved with the 3D-NPMg anode compared with conventional Mg foils. Our results highlight the critical importance of structural design for enabling stable and efficient MMBs. The adaptability of this method to various metals with tunable nanoscale features underscores its broad potential for advanced energy storage applications.

Experimental Methods

Synthesis of Three-Dimensional Nanoporous Mg (3D-NPMg) Metal

3D-NPMg was prepared as previously reported.[17] All reactions were carried out in an Ar-filled glove box. Prior to use, all glassware and magnetic stirring bars were heated at 100 °C, and the tetrahydrofuran (THF, 99.5%, DAEJUNG Chemical) used as the solvent was highly purified through a solvent purification system. For the synthesis, an Mg$_{15}$Li$_{85}$ alloy foil (1 mm thick, NEBA Corporation) was cut into circular discs (12 mm in diameter) with an approximate mass of 80 mg. To remove surface passivation, the alloy discs were polished with a 20 mg mL^{-1} solution of naphthalene (99%, Sigma-Aldrich) in THF. After surface polishing, each disc was added to a reaction

vessel containing 88 mL of a 20 mg mL^{-1} naphthalene solution in THF and stirred at 600 rpm for 72 h. Upon completion, the de-alloyed disc was washed twice with THF to dissolve any remaining reactants or liquid-state products and dried under dynamic vacuum overnight.

Electrode and Cell Preparations

CR2032 coin cells were assembled in an Ar-filled glove box. Each cell used a 3D-NPMg disc as the counter electrode and a polished Mg foil (0.1 mm thick, >99.95%, Hanaro TR) as the reference electrode. Glass fiber (GF/F, Whatman) served as the separator, and an all-phenyl complex (APC) was used as the electrolyte. The APC electrolyte was synthesized by first adding 1 M aluminum chloride (AlCl$_3$, 99.99%, Sigma-Aldrich) to THF (99.9%, Sigma-Aldrich) and stirring the mixture at room temperature for 12 h. A 2.0 M solution of phenyl magnesium chloride (PhMgCl, Sigma-Aldrich) in THF was then added, and stirring was continued for another 12 h. All of the synthesis steps were performed in a glove box, and the reagents were pre-dried for 24 h to remove traces of moisture.

Characterizations

SEM images were obtained using an SU8230 instrument (Hitachi, KARA). To minimize the charging effect and enhance the resolution, a Pt coating (3 mA for 1 min) was applied immediately before imaging. Transmission electron micrographs and elemental mapping images were obtained using a Talos F200X instrument (Thermo Fisher, KARA) operated at 200 kV. The 3D nanoporous samples were crushed, followed by ultrasonication for 1 h. Subsequently, the supernatant was dropped onto a lacey carbon grid, and the grid was dried under vacuum to remove contaminants adsorbed to the surface of the sample. The grid was briefly exposed to air during the transfer process before the sample holder was inserted into the TEM instrument. The phase and structure of the metal surface were recorded using X-ray diffraction (XRD; Bruker, D6 phaser) with a Cu K$_a$ radiation ($\lambda = 1.5406$ Å). X-ray photo-electron spectra (XPS) were collected using a K-alpha X-ray photo-electron spectrometer (Thermo VG Scientific, KARA) with Al as the X-ray source (1486.7 eV) under ultra-high vacuum (UHV) conditions ($< 10^{-9}$ Torr). The collected spectra were calibrated using the adventitious C 1s peak at 285 eV as a standard. To prevent contamination from air, the samples were loaded into an XPS vacuum-transfer module in an Ar-filled glove box. The N$_2$ sorption isotherms were obtained using an ASAP2020 instrument (Micromeritics). Approximately 200 mg of sample was loaded into a quartz tube in an Ar-filled glovebox and sealed with parafilm when transferred to the instrument. The samples were degassed at 80 °C before N$_2$ sorption isotherms were collected.

Conflict of Interests

The authors declare that they have American, Japanese, German, Saudi Arabian, Chinese, and Korean patent applications related to this work.

Data Availability Statement

The data that support the findings of this study are available from the corresponding author upon reasonable request.

[1] a) B. Dunn, H. Kamath, J.-M. Tarascon, *Science* **2011**, *334*, 928–935; b) G. Harper, R. Sommerville, E. Kendrick, L. Driscoll, P. Slater, R. Stolkin, A. Walton, P. Christensen, O. Heidrich, S. Lambert, *Nature* **2019**, *575*, 75–86.

[2] a) R. K. Guduru, J. C. Icaza, *Nanomaterials* **2016**, *6*, 41; b) J. E. Huheey, E. A. Keiter, R. L. Keiter, O. K. Medhi, *Inorganic chemistry: principles of structure and reactivity*, Prentice Hall, Upper Saddle River, **1997**

[3] a) D. Aurbach, Z. Lu, A. Schechter, Y. Gofer, H. Gizbar, R. Turgeman, Y. Cohen, M. Moshkovich, E. Levi, *Nature* **2000**, *407*, 724–727; b) G. Fang, J. Zhou, A. Pan, S. Liang, *ACS Energy Lett.* **2018**, *3*, 2480–2501; c) M.-C. Lin, M. Gong, B. Lu, Y. Wu, D.-Y. Wang, M. Guan, M. Angell, C. Chen, J. Yang, B.-J. Hwang, *Nature* **2015**, *520*, 324–328; d) J. Zheng, S. Chen, W. Zhao, J. Song, M. H. Engelhard, J.-G. Zhang, *ACS Energy Lett.* **2018**, *3*, 315–321.

[4] a) C. Wei, L. Tan, Y. Zhang, Z. Wang, J. Feng, Y. Qian, *Energy Storage Mater.* **2022**, *52*, 299–319; b) F. Liu, T. Wang, X. Liu, L. Z. Fan, *Adv. Energy Mater.* **2021**, *11*, 2000787.

[5] H. D. Yoo, I. Shterenberg, Y. Gofer, G. Gershinsky, N. Pour, D. Aurbach, *Energy Environ. Sci.* **2013**, *6*, 2265–2279.

[6] T. D. Gregory, R. J. Hoffman, R. C. Winterton, *J. Electrochem. Soc.* **1990**, *137*, 775.

[7] G. Gershinsky, H. D. Yoo, Y. Gofer, D. Aurbach, *Langmuir* **2013**, *29*, 10964–10972.

[8] O. Mizrahi, N. Amir, E. Pollak, O. Chusid, V. Marks, H. Gottlieb, L. Larush, E. Zinigrad, D. Aurbach, *J. Electrochem. Soc.* **2007**, *155*, A103.

[9] R. E. Doe, R. Han, J. Hwang, A. J. Gmitter, I. Shterenberg, H. D. Yoo, N. Pour, D. Aurbach, *Chem. Commun.* **2014**, *50*, 243–245.

[10] R. Mohtadi, M. Matsui, T. S. Arthur, S.-J. Hwang, *Angew. Chem. Int. Ed.* **2012**, *51*, 9780.

[11] a) I. Kedrinsky, I. Murygin, V. Dmitrenko, O. Abolin, G. Sukhova, I. Grudyanov, *J. Power Sources* **1988**, *22*, 99–114; b) T. Wen, Y. Deng, B. Qu, G. Huang, J. Song, C. Xu, A. Du, Q. Xie, J. Wang, G. Cui, *ACS Energy Lett.* **2023**, *8*, 4848–4861; c) R. Davidson, A. Verma, D. Santos, F. Hao, C. Fincher, S. Xiang, J. Van Buskirk, K. Xie, M. Pharr, P. P. Mukherjee, *ACS Energy Lett.* **2018**, *4*, 375–376; d) J. H. Kwak, Y. Jeoun, S. H. Oh, S. Yu, J.-H. Lim, Y.-E. Sung, S.-H. Yu, H.-D. Lim, *ACS Energy Lett.* **2021**, *7*, 162–170.

[12] a) S.-B. Son, T. Gao, S. P. Harvey, K. X. Steirer, A. Stokes, A. Norman, C. Wang, A. Cresce, K. Xu, C. Ban, *Nat Chem.* **2018**, *10*, 532–539; b) Y. Y. Hwang, N. K. Lee, S. H. Park, J. Shin, Y. J. Lee, *Energy Storage Mater.* **2022**, *51*, 108–121; c) J. Zhang, X. Guan, R. Lv, D. Wang, P. Liu, J. Luo, *Energy Storage Mater.* **2020**, *26*, 408–413; d) G. Li, K. Chen, M. Lei, T. Wang, M. Hu, C. Li, *Adv. Energy Mater.* **2024**, *14*, 2401507; e) M. Hu, G. Li, K. Chen, X. Zhou, C. Li, *Chem. Eng. J.* **2024**, *480*, 148193; f) G. Li, Y. Li, M. Lei, K. Chen, C. Li, *Small* **2024**, *20*, 2405568; g) Y. Li, X. Zhou, J. Hu, Y. Zheng, M. Huang, K. Guo, C. Li, *Energy Storage Mater.* **2022**, *46*, 1–9.

[13] a) J. H. Kwak, S. Shin, Y. Jeoun, Y. Lee, S. Yu, Y. S. Yun, Y.-E. Sung, S.-H. Yu, H.-D. Lim, *J. Power Sources* **2022**, *541*, 231724; b) H.-D. Lim, D. H. Kim, S. Park, M. E. Lee, H.-J. Jin, S. Yu, S. H. Oh, Y. S. Yun, *ACS Appl. Mater. Interfaces* **2019**, *11*, 38754–38761; c) Z. Song, Z. Zhang, A. Du, S. Dong, G. Li, G. Cui, *Adv. Mater.* **2021**, *33*, 2100224; d) J. Liu, J. Zhang, Z. Zhang, A. Du, S. Dong, Z. Zhou, X. Guo, Q. Wang, Z. Li, G. Li, *ACS Nano* **2022**, *16*, 9894–9907.

[14] Y. An, Y. Tian, C. Liu, S. Xiong, J. Feng, Y. Qian, *ACS Nano* **2022**, *16*, 4560–4577.

Batteries & Supercaps

Research Article
doi.org/10.1002/batt.202400749

Chemistry Europe
European Chemical
Societies Publishing

[15] a) W. Campbell, U. Thomas, *Trans. Electrochem. Soc.* **1947**, *91*, 623; b) T. Juarez, J. Biener, J. Weissmüller, A. M. Hodge, *Adv. Eng. Mater* **2017**, *19*, 1700389.

[16] a) A. Maddegalla, A. Mukherjee, J. A. Blázquez, E. Azaceta, O. Leonet, A. R. Mainar, A. Kovalevsky, D. Sharon, J. F. Martin, D. Sotta, *ChemSusChem* **2021**, *14*, 4690–4696; b) M. Bockelmann, L. Reining, U. Kunz, T. Turek, *Electrochim. Acta* **2017**, *237*, 276–298.

[17] Y. Cho, A. J. E. Rowberg, S. Chatterjee, A. Jamal, S. Kang, T. W. Heo, B. C. Wood, E. S. Cho, **2024**, *Status: Submitted*.

[18] O. Friedrichs, J. Sánchez-López, C. López-Cartes, M. Dornheim, T. Klassen, R. Bormann, A. Fernández, *Appl. Surf. Sci.* **2006**, *252*, 2334–2345.

[19] N. G. Connelly, W. E. Geiger, *Chem. Rev.* **1996**, *96*, 877–910.

[20] J. Fu, J. S. Corsi, S. S. Welborn, V. Basile, L. Wang, A. K. Ng, E. Detsi, *ACS Sustain. Chem. Eng.* **2021**, *9*, 2762–2769.

[21] M. S. Ding, T. Diemant, R. J. Behm, S. Passerini, G. A. Giffin, *J. Electrochem. Soc.* **2018**, *165*, A1983.

[22] J. Bi, Z. Zhou, J. Li, B. Li, X. Sun, Y. Liu, K. Wang, G. Gao, Z. Du, W. Ai, *Angew. Chem. Int. Ed.* **2024**, *63*, e202407770.

[23] a) J. Lin, Z. Wang, W. Ke, X. He, P. Liang, C. Zhang, *Intermetallics* **2024**, *170*, 108308; b) Y. Wang, Y. Zhang, X. Liu, J. Wang, X. Xie, J. Jiang, J. Liu, H. Liu, Y. Wu, S. Dong, *Crystals* **2022**, *12*, 1305.

[24] a) L. Wang, N. J. Briot, P. D. Swartzentruber, T. J. Balk, *Metall. Mater. Trans. A* **2014**, *45*, 1–5; b) K. Thool, K. Yazar, V. Kavimani, A. Gupta, S.-H. Choi, *Crystals* **2024**, *14*, 727.

[25] F. Wang, D. Wu, Y. Zhuang, J. Li, X. Nie, J. Zeng, J. Zhao, *ACS Appl. Mater. Interfaces* **2022**, *14*, 31148–31159.

[26] M. Thommes, K. Kaneko, A. V. Neimark, J. P. Olivier, F. Rodriguez-Reinoso, J. Rouquerol, K. S. Sing, *Pure Appl. Chem.* **2015**, *87*, 1051–1069.

[27] C. Coaty, H. Zhou, H. Liu, P. Liu, *ACS Nano* **2018**, *12*, 432–440.

[28] a) J. Chang, R. T. Haasch, J. Kim, T. Spila, P. V. Braun, A. A. Gewirth, R. G. Nuzzo, *ACS Appl. Mater. Interfaces* **2015**, *7*, 2494–2502; b) S. Kúdela, S. Oswald, S. Kúdela Jr, S. Baunack, K. Wetzig, *Microchimica Acta* **2000**, *133*, 29–34.

[29] T. Fujita, P. Guan, K. McKenna, X. Lang, A. Hirata, L. Zhang, T. Tokunaga, S. Arai, Y. Yamamoto, N. Tanaka, *Nat. Mater.* **2012**, *11*, 775–780.

[30] Z. Liang, C. Ban, *Angew. Chem. Int. Ed.* **2021**, *60*, 11036–11047.

[31] a) C. S. Santos, M. Romio, Y. Surace, N. Eshraghi, M. Amores, A. Mautner, C. Groher, M. Jahn, E. Ventosa, W. Schuhmann, *Chem. Sci.* **2023**, *14*, 9923–9932; b) V. B. Parambath, Z. Zhao-Karger, T. Diemant, M. Jäckle, Z. Li, T. Scherer, A. Gross, R. J. Behm, M. Fichtner, *J. Mater. Chem. A* **2020**, *8*, 22998–23010.

[32] Y. Liu, X. Xu, M. Sadd, O. O. Kapitanova, V. A. Krivchenko, J. Ban, J. Wang, X. Jiao, Z. Song, J. Song, *Adv. Sci.* **2021**, *8*, 2003301.